Electron-nuclear interactions as a test of crystal field parameters for low-symmetry systems: Zeeman hyperfine spectroscopy of Ho³⁺-doped Y₂SiO₅

Sagar Mothkuri,[1,2] Michael F. Reid ®,[1,2,*] Jon-Paul R. Wells ®,[1,2,†] Eloïse Lafitte-Houssat,[3,4] Philippe Goldner,[3] and Alban Ferrier[3,5]

[1]*School of Physical and Chemical Sciences, University of Canterbury, PB 4800, Christchurch 8140, New Zealand*
[2]*The Dodd-Walls Centre for Photonic and Quantum Technologies, Dunedin 9016, New Zealand*
[3]*Chimie ParisTech, PSL University, CNRS, Institut de Recherche de Chimie Paris, 75005 Paris, France*
[4]*Thales Research and Technology, 1 Avenue Augustin Fresnel, 91767 Palaiseau, France*
[5]*Faculté des Sciences et Ingénierie, Sorbonne Université, UFR 933, 75005 Paris, France*

High-resolution Zeeman spectroscopy of electronic-nuclear hyperfine levels of $^5I_8 \rightarrow {}^5I_7$ transitions in Ho³⁺:Y₂SiO₅ is reported. Crystal-field parameters determined for the two C_1 symmetry sites in Er³⁺:Y₂SiO₅ are successfully used to model the Zeeman-hyperfine data, including the prediction of avoided crossings between hyperfine levels under the influence of an external magnetic field. The two six- and seven-coordinate substitutional sites may be distinguished by comparing the spectra with crystal-field calculations.

I. INTRODUCTION

Yttrium orthosilicate (Y₂SiO₅) doped with rare-earth ions is widely seen as an attractive option for the development of quantum-information technologies. The magnetic moment of yttrium is very small and isotopes of Si and O with nonzero nuclear spin have very low natural abundances. Consequently, decoherence due to spin flips is low, giving outstanding coherence properties. Furthermore, the substitutional sites for rare-earth ions in Y₂SiO₅ have C_1 point-group symmetry, giving highly admixed wave functions, which enables efficient and diverse optical pumping schemes [1–3]. Applications include optical quantum memories [4–9], quantum-gate implementations [1,3], microwave-to-optical photon modulators [10,11], and single-photon sources [12]. Recently, control of multiple ions at the single-photon level has been demonstrated [13].

Performance improvements for such technologies require highly accurate modeling of magnetic-hyperfine structure to determine optimized regions where the Zero-First-Order-Zeeman (ZEFOZ) technique can be most efficiently exploited. Use of the ZEFOZ technique has already enabled the demonstration of a spin coherence time of 6 h in ^{151}Eu³⁺: Y₂SiO₅ [5].

Crystal-field calculations [14–17] may be used to model the electronic structure of the entire $4f^N$ configuration of a rare-earth ion. Since the crystal-field parameters vary in a systematic way across the rare-earth series, the information they carry may be transferred between different ions. However, the determination of crystal-field parameters for crystals where the rare-earth ions occupy low point-group symmetry sites is nontrivial. Additional information from magnetic splittings is essential to provide the orientation information necessary to determine a unique set of parameters [18,19]. In C_1 symmetry (i.e., no symmetry), there are 27 crystal-field parameters, so the calculations are computationally challenging. However, recently we have developed techniques that make it practical to obtain full phenomenological crystal-field fits for C_1 point-group symmetry sites. These methods have been applied to both sites of Er³⁺:Y₂SiO₅ [20,21] with considerable success. These parameters have also been applied to the Zeeman splittings of Nd³⁺ and Sm³⁺ ions in Y₂SiO₅ [22], demonstrating that the parameters may be transferred from ion to ion, and that the two six- and seven-coordinate substitutional sites may be distinguished by comparing calculations with experiment.

The Nd³⁺ and Sm³⁺ work did not include nuclear hyperfine measurements. In this work, we utilize the large magnetic moment and high nuclear spin ($I = 7/2$) of the trivalent holmium ion, and the application of magnetic fields, to explore the predictive ability of crystal-field calculations in the context of Zeeman-hyperfine measurements. This analysis is directly relevant to the utilization of the ZEFOZ technique in quantum information storage.

II. EXPERIMENTAL

Y₂SiO₅ (in the X2 phase) is a monoclinic crystal with C_{2h}^6 space group symmetry. The yttrium ions occupy two crystallographically distinct sites, each with C_1 point-group symmetry, with oxygen coordination numbers of six and seven [23]. We follow the labeling convention used in Er³⁺ [21,24] and in Ref. [22] of referring to these as Site 1 and Site 2, tentatively identified as six- and seven-coordinate. Y₂SiO₅ has three perpendicular optical-extinction axes: the crystallographic b axis and two mutually perpendicular axes labeled D_1 and D_2. In

*Corresponding author: mike.reid@canterbury.ac.nz
†Corresponding author: jon-paul.wells@canterbury.ac.nz

our calculations we follow the convention of identifying these as the *z*, *x*, and *y* axes, respectively [24].

The crystal of Ho^{3+}:Y_2SiO_5 used in the current study was prepared using the Czochralski process with a Ho^{3+} concentration of 200 ppm. The crystal was oriented using Laue backscattering. The sample was a cuboid with the D_1 and D_2 and *b* axes through the faces and dimensions of approximately 5 mm on each side. The sample was given a spectroscopic quality polish exhibiting excellent optical quality.

Infrared absorption spectroscopy was performed using a Bruker Vertex 80 FTIR having its entire optical path purged by N_2 gas. This instrument has a maximum apodized resolution of 0.075 cm^{-1} (2.2 GHz). Zeeman measurements were performed using a 4 T, superconducting, simple solenoid built into a homebuilt cryostat. The sample is mounted on a screw fitted into the bore of the solenoid and is therefore cooled by thermal contact with the 4.2 K helium bath of the solenoid.

III. THEORETICAL BACKGROUND

The Hamiltonian for the $4f^N$ configuration may be written as [14,15,17]

$$H = H_{FI} + H_{CF} + H_{HF} + H_Z. \tag{1}$$

The terms in this equation represent the free-ion contribution, the crystal-field interaction, the electron-nuclear hyperfine interaction, and the Zeeman interaction.

The free-ion Hamiltonian may be written as

$$H_{FI} = E_{avg} + \sum_{k=2,4,6} F^k f_k + \zeta \sum_i \mathbf{s}_i \cdot \mathbf{l}_i$$

$$+ \alpha L(L+1) + \beta G(G_2) + \gamma G(R_7) + \sum_{k=2,3,4,6,7,8} T^k t_k$$

$$+ \sum_{k=0,2,4} M^k m_k + \sum_{k=2,4,6} P^k p_k. \tag{2}$$

E_{avg} is a constant configurational shift, F^k Slater are parameters characterizing aspherical electrostatic repulsion, and ζ the spin-orbit coupling constant. The sum in the spin-orbit term is over the $4f$ electrons. The other terms parametrize two- and three-body interactions, as well as higher-order spin-dependent effects [14,17].

The crystal-field Hamiltonian has the form

$$H_{CF} = \sum_{k,q} B_q^k C_q^{(k)}, \tag{3}$$

with $k = 2$, 4, 6, $q = -k, \dots, k$. The B_q^k are crystal field parameters; $C_q^{(k)}$ are spherical tensor operators. In C_1 symmetry, all nonaxial ($q \neq 0$) B_q^k parameters are complex, leading to a total of 27 parameters. Due to this low symmetry, all electronic states are nondegenerate in Ho^{3+}.

The holmium nucleus has a spin $I = 7/2$, and the electronic states are coupled to the nuclear spins by the hyperfine interaction, giving 8 electronic-nuclear states for each electronic level. We use basis states $|JM_J, IM_I\rangle$ in our calculations.

For holmium the magnetic-hyperfine interaction is much larger than the nuclear-quadrupole interaction [25], so here we
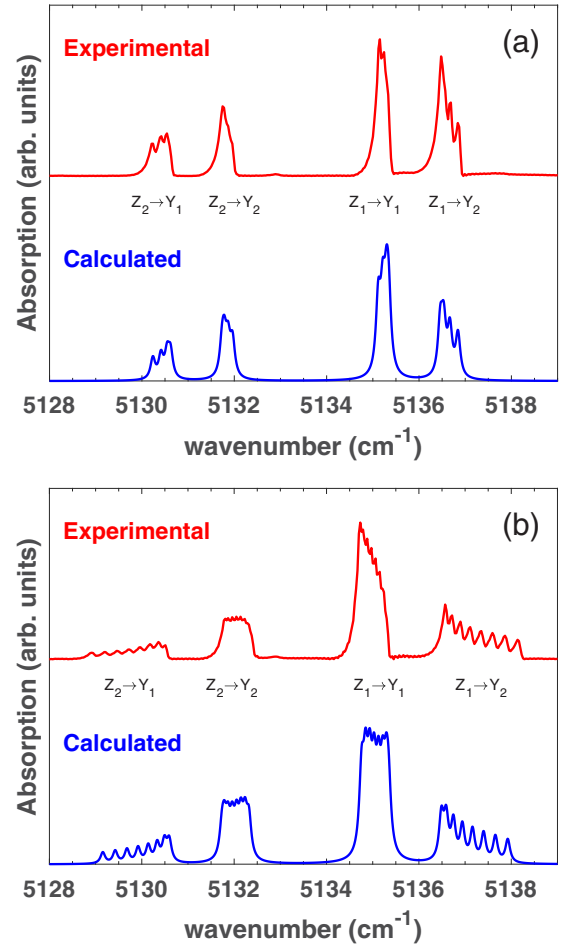

FIG. 1. The 4.2 K absorption spectrum of the Z_1-$Z_2 \longrightarrow Y_1$-Y_2 transitions for Site 2 of Ho^{3+}:Y_2SiO_5. (a) Zero-field spectrum and (b) 0.3 T spectrum with a magnetic field applied along the *b* axis.

consider only the magnetic hyperfine part of the Hamiltonian, which within a single multiplet may be written as

$$H_{HF} = A_J \mathbf{J} \cdot \mathbf{I}, \tag{4}$$

where A_J is the hyperfine coupling constant for the multiplet. The A_J may be calculated using eigenvectors of the free-ion part of the Hamiltonian.

The effect of an external magnetic field is given by the Zeeman Hamiltonian

$$H_Z = \mu_B \mathbf{B} \cdot (\mathbf{L} + 2\mathbf{S}), \tag{5}$$

where B is the magnetic field. Within a multiplet $\mathbf{L} + 2\mathbf{S}$ may be written as a g factor $g(^{2S+1}L_J)$ multiplied by $\mathbf{J}$.

IV. RESULTS AND DISCUSSION

Figure 1 shows the lowest-energy $^5I_8$ (Z) $\longrightarrow$ $^5I_7$ (Y) absorption transitions, which we assign to Site 2 (see below). Both the ground and the excited states are closely spaced electronic singlets, which can be observed as four sets of transitions in Fig. 1(a). At low temperatures, the population of Z_2 is significantly less than that of Z_1. Though the sample is in contact with a mount that is nominally at 4.2 K, a comparison of intensity ratios with the Boltzmann equation suggests

TABLE I. Experimental and calculated Z_1-$Z_2 \longrightarrow Y_1$-Y_2 transition energies for Site 2. All values are in units of cm^{-1}.

Transition	Experimental	Calculated
Z_2-Y_1	5130.22	5130.23
	5130.41	5130.41
	5130.54	5130.54
	5130.61	5130.62
Z_2-Y_2	5131.68	5131.73
	5131.76	5131.78
	5131.87	5131.87
	5131.95	5131.96
Z_1-Y_1	5135.09	5135.11
	5135.14	5135.21
	5135.24	5135.29
	5135.32	5135.34
Z_1-Y_2	5136.46	5136.45
	5136.49	5136.53
	5136.68	5136.66
	5136.84	5136.84

that the sample temperature is close to 10 K. The close proximity of these levels, together with the low point-group symmetry of the Ho^{3+} ions, suggests we may treat these levels as a pair of pseudodoublets, with their close proximity giving significant magnetic interactions such as Zeeman-hyperfine effects. Indeed, the zero-field spectrum shown in Fig. 1(a) exhibits partially resolved hyperfine splittings significantly larger than the inhomogeneous broadening of the spectral lines. Estimated transition energies are listed in Table I. Figure 1(b) shows the same transitions with the application of a 0.3 T magnetic field along the b axis.

We model the spectrum by first calculating electronic energy levels and wave functions and then treating the hyperfine interaction as a perturbation. Table II gives calculated energies for the lowest two ${}^5I_8$ (Z_1, Z_2) and ${}^5I_7$ (Y_1, Y_2) states. These calculations use the crystal-field parameters for Er^{3+} in Y_2SiO_5 from Ref. [20] for Site 1 and Site 2 and the free-ion parameters for Ho^{3+} from Ref. [14]. The Y_1 and Y_2 levels for Site 2 are calculated to be lower than those for Site 1, so we assign the spectrum in Fig. 1 to Site 2. The calculated splitting between Z_1 and Z_2 and the splitting between Y_1 and

TABLE II. Energy levels for the Z_1, Z_2, Y_1, and Y_2 states for Site 1 and Site 2 from crystal-field calculations (CF) and after fitting to the experimental data. The last row shows the splitting between Y_1 and Y_2. All values in units of cm^{-1}.

Multiplet	Energy level	Site 1		Site 2	
		CF	Fit	CF	Fit
${}^5I_8$	Z_1	0	0	0	0
	Z_2	4.67	4.87	1.77	4.72
${}^5I_7$	Y_1	5162.19	5158.20	5125.37	5135.25
	Y_2	5162.70	5159.25	5125.92	5136.40
	$\Delta_{Y_1Y_2}$	0.51	1.05	0.55	1.15

TABLE III. Absolute values of matrix elements of the angular momentum operators from crystal-field calculations. The diagonal matrix elements are not shown, but are of the order of 10^{-4}.

Energy level	Site 1			Site 2		
	J_x	J_y	J_z	J_x	J_y	J_z
$|\langle Z_1|J_i|Z_2\rangle|$	2.53	5.34	1.47	3.01	2.75	5.12
$|\langle Y_1|J_i|Y_2\rangle|$	1.96	5.19	2.15	3.01	2.76	4.9924

Y_2 are smaller than the experimental splitting, so we treat the energies as adjustable parameters.

Table III gives the relevant matrix elements of the angular momentum operators J_x, J_y, and J_z calculated using eigenvectors from the crystal-field calculation. These operators contribute to both the hyperfine splitting [Eq. (4)] and the magnetic splitting [Eq. (5)]. The different magnitudes of the matrix elements of these operator for the two sites, and the different directions, will allow us to confirm our assignments. The A and g factors for the relevant multiplets are given in Table IV. The only free parameters in our calculation are the energies of Z_1, Z_2, Y_1, and Y_2. These fitted energies are given in Table II.

The addition of the nuclear spin ($I = 7/2$) expands each singlet electronic state into 8 electronic-nuclear states. However, due to Kramers degeneracy, in the absence of a magnetic field there are only four distinct energies for each electronic state. Thus, there are two 16×16 matrices, one each for the Z_1-Z_2 and Y_1-Y_2 states. Since the diagonal matrix elements of **J** are extremely small (they would be zero for isolated singlets), it is the off-diagonal matrix elements of $A_J \mathbf{J} \cdot \mathbf{I}$ between Z_1 and Z_2 or Y_1 and Y_2 that are responsible for the hyperfine splitting. Figure 2 shows the calculated zero-field energy levels and the calculated transition energies are given in Table I. Figure 3 shows the energies as a function of magnetic field.

The eigenvectors from the electronic-hyperfine calculation can also be used to estimate the absorption. The ${}^5I_8$ to ${}^5I_7$ transitions are predominantly magnetic dipole [25] in nature. The calculated spectra in Fig. 1 were obtained by calculating the squares of the appropriate magnetic-dipole moments and adding line profiles of width (FWHM) $0.12 \ cm^{-1}$.

In the low-symmetry sites of Y_2SiO_5, the hyperfine Hamiltonian [Eq. (4)] mixes states with different M_I. This is in contrast to the high-symmetry sites in Refs. [25,26], where the states are pure M_I. Since optical transitions do not change the nuclear spin, in the high-symmetry systems the number of allowed transitions is restricted, and at zero field there are

TABLE IV. Hyperfine and magnetic constants calculated using eigenvectors of the free-ion part of the Hamiltonian [25].

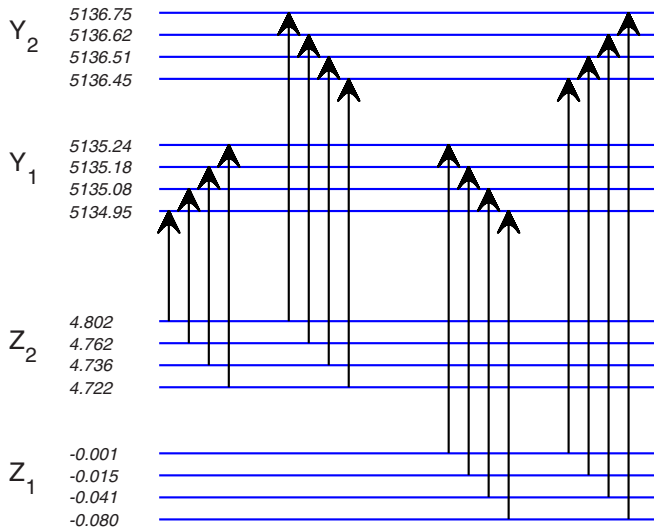| Constant	Value
$A({}^5I_8)$	812 MHz
$A({}^5I_7)$	883 MHz
$g({}^5I_8)$	1.24
$g({}^5I_7)$	1.17

FIG. 2. Calculated hyperfine energy level structure for Site 2 of $Ho^{3+}:Y_2SiO_5$. Vertical arrows show the strong transitions between Z_1-Z_2 and Y_1-Y_2.

FIG. 3. Calculated Zeeman-hyperfine energy level structure for Site 2 of $Ho^{3+}:Y_2SiO_5$ with a magnetic field applied along the *b* axis. Vertical arrows show the strong transitions between Z_1-Z_2 and Y_1-Y_2.

only four distinct transitions between singlet electronic states. Our spectra, and our calculations, also give only four strong transitions at zero field, even though in principle all possible transitions are allowed. This is because the eigenvectors of the hyperfine Hamiltonian for Z_1-Z_2 and Y_1-Y_2 are sufficiently similar that only four transitions with distinct energies at zero field, and 8 at nonzero field, have significant intensity.

Experimental data and calculations for the magnetic field range from 0 to 0.5 T are shown in Fig. 4. With the aid of Fig. 3, which indicates the approximate selection rules, it is clear why the $Z_1 \longrightarrow Y_2$ and $Z_2 \longrightarrow Y_1$ transitions move apart, and the $Z_1 \longrightarrow Y_1$ and $Z_2 \longrightarrow Y_2$ transitions move together as the field increases. In the latter case the energy *differences* tend toward the same value. A similar calculation also reproduces the magnetic splitting along the D_2 axis. The matrix elements of J_y are smaller than those of J_z (Table III), so both experimental and calculated magnetic splittings are smaller. Note, also, that the J_z matrix elements are significantly smaller for Site 1, and if the Site 1 eigenvectors were used, the calculation would be in poor agreement with the experimental measurements. Thus, the calculations confirm our site assignment.

Anticrossings between magnetic-hyperfine levels are of interest in quantum-information applications, since transitions at those points suffer minimal effects of magnetic fluctuations [5,27]. Figure 5 gives a blowup of our calculated Z_1 and Z_2 states. As the magnetic field is increased, anticrossings between the Z_1 and the Z_2 states are apparent. These are the order of 4.7 cm^{-1} (140 GHz). This splitting is much larger than the 9 GHz splitting utilized in the EPR experiments of Ref. [27], due to the much larger matrix elements of **J** connecting the Z_1 and Z_2 states in our system. Consequently, the second derivatives with respect to changes in the magnetic field are considerably smaller in our system.

There are also anticrossings between the Z_1 states. These are not resolved in Fig. 5, since the spacings at the anticrossings range from 2 to 9 MHz. These spacings are small
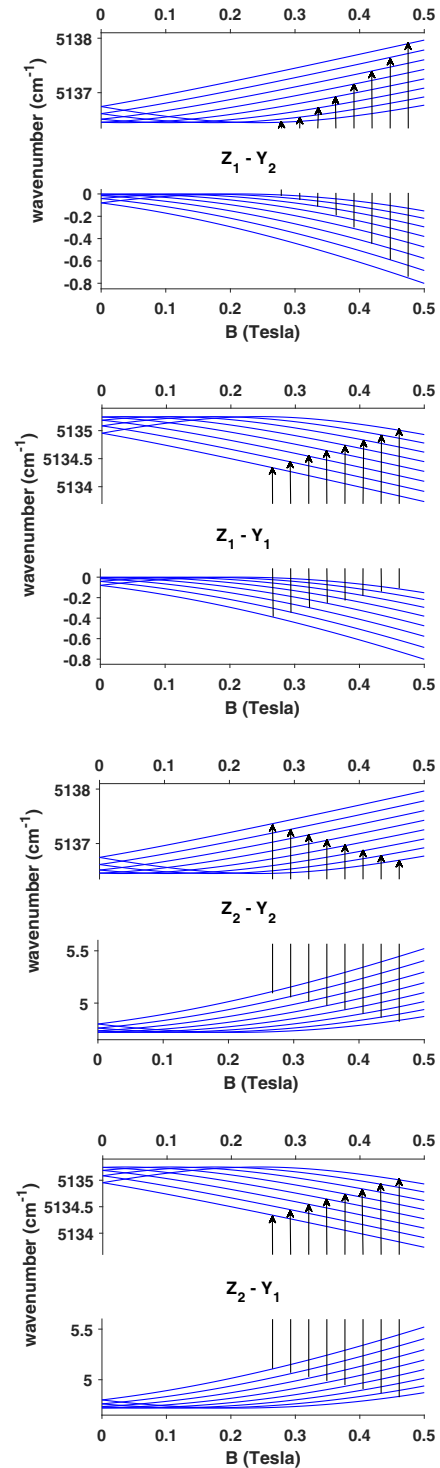
because the matrix elements of **J** within Z_1 are the order of 10^{-4} cm^{-1}, which is a result of the electronic states being nondegenerate. In Ref. [26], anticrossings of approximately 1.8 GHz were observed by infrared absorption in a degenerate excited state of Ho^{3+} in $LiYF_4$. The hyperfine anticrossings
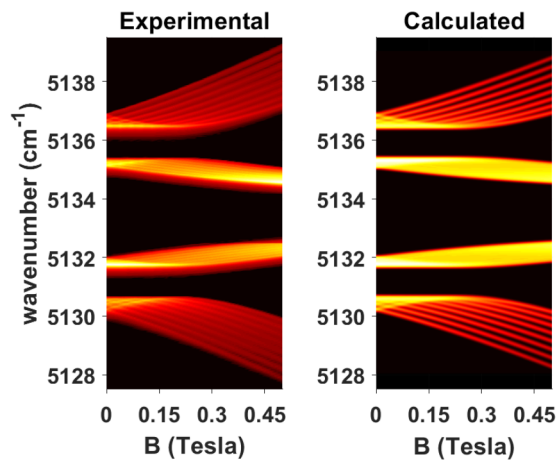
FIG. 4. Map of the experimental and calculated Zeeman-hyperfine infrared absorption spectra for the Z_1-$Z_2 \longrightarrow Y_1$-Y_2 transitions of Site 2 for Ho^{3+}:Y_2SiO_5 with a magnetic field applied along the b axis.

in the nondegenerate electronic states of Ho^{3+}:Y_2SiO_5 are too small to resolve by optical absorption measurements.

We now consider a region that we assign to transitions of Ho^{3+} in Site 1. In Figs. 6 and 7, experimental data are compared with calculations of hyperfine and magnetic splittings for Z_1-$Z_2 \longrightarrow Y_1$-Y_2 transitions of Site 1. This region also contains lines that we assign to Site 2 and to water (indicated by asterisks). For clarity, these features were removed from Fig. 7. The hyperfine structure is not fully resolved, but it is clear that both measured and calculated Zeeman splittings are much smaller for Site 1 than for Site 2. Though the calculation reproduces the experimental *energies*, it does not accurately reproduce the experimental *intensities* under the influence of a magnetic field [Fig. 6(b)]. It is possible that mixing with higher-lying electronic states is responsible for this discrepancy. To properly account for such effects would require going beyond the perturbation approach used here to a calculation taking into account the crystal-field, hyperfine, and Zeeman interactions for the full $4f^{10}$ configuration.
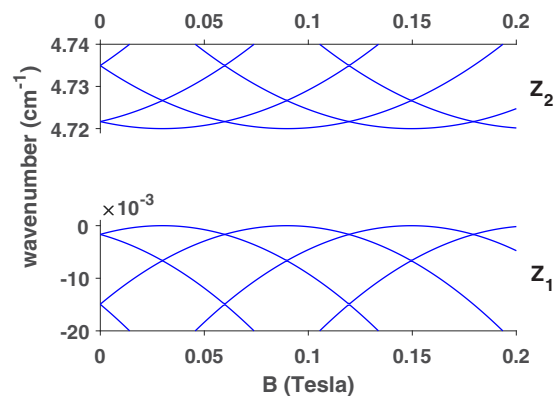

FIG. 5. Calculated anticrossings in the Z_1-Z_2 region of Site 2 with a magnetic field applied along the b axis. The energy gaps at the anticrossing points *within* Z_1 and Z_2 are the order of 10^{-4} cm^{-1} (5MHz), so are not visible in the figure.
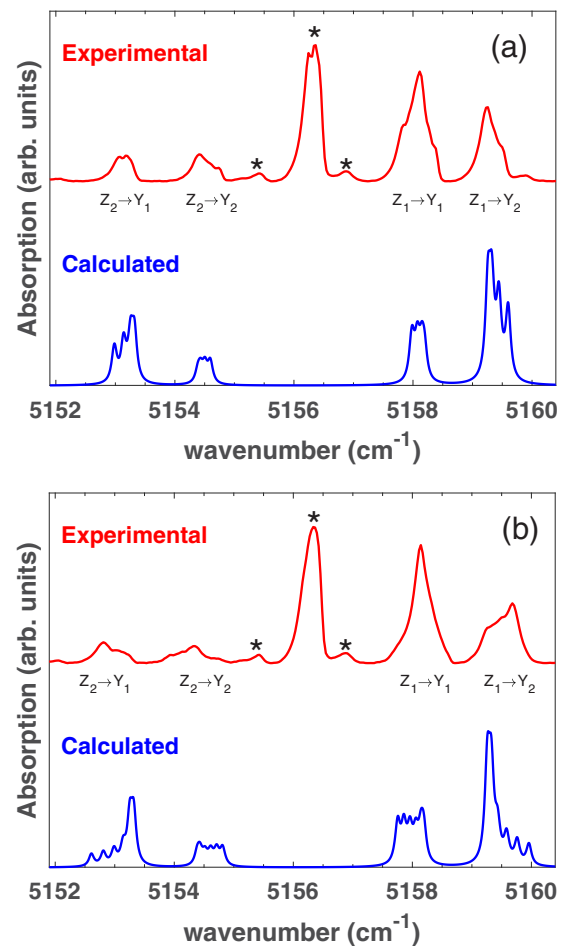

FIG. 6. 4.2 K absorption spectrum of the Z_1-$Z_2 \longrightarrow Y_1$-Y_2 transitions for Site 1 of Ho^{3+}:Y_2SiO_5. (a) Zero-field spectrum and (b) 0.3 T spectrum with a magnetic field applied along the b axis. Asterisks indicate transitions assigned to Site 2 (the largest feature) and water.
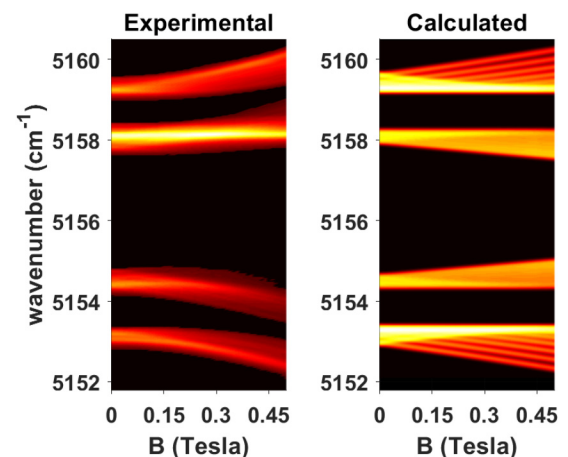

FIG. 7. Map of the experimental and calculated Zeeman-hyperfine infrared absorption spectra for the Z_1-$Z_2 \longrightarrow Y_1$-Y_2 transitions of Site 1 for Ho^{3+}:Y_2SiO_5 with a magnetic field applied along the b axis. For clarity, transitions assigned to Site 2 and water have been deleted from the experimental map.

V. CONCLUSIONS

We have presented Zeeman-hyperfine spectra for the lowest energy infrared absorption transitions of Ho^{3+} doped into high-quality Y_2SiO_5 crystals. We have demonstrated that the data may be modeled using electron-nuclear wave functions derived from a Ho^{3+} crystal-field calculation using parameters obtained previously for the Er^{3+} ion, which neighbors Ho^{3+} in the periodic table. The results presented here form an important test of both the transferability of parameters from ion-to-ion and the predictive ability of crystal-field calculations for sites exhibiting very low C_1 point group symmetry. The calculations are, therefore, an important step in establishing a consistent set of crystal-field parameters for rare-earth ions in Y_2SiO_5. It is notable that not only are our calculations able to distinguish spectroscopic features of the two substitutional sites but also, in fact, give excellent agreement with few fitting parameters.

[1] L. Rippe, B. Julsgaard, A. Walther, Y. Ying, and S. Kröll, Phys. Rev. A **77**, 022307 (2008).

[2] B. Lauritzen, S. R. Hastings-Simon, H. de Riedmatten, M. Afzelius, and N. Gisin, Phys. Rev. A **78**, 043402 (2008).

[3] J. J. Longdell and M. J. Sellars, Phys. Rev. A **69**, 032307 (2004).

[4] H. de Riedmatten, M. Afzelius, M. U. Staudt, C. Simon, and N. Gisin, Nature **456**, 773 (2008).

[5] M. Zhong, M. P. Hedges, R. L. Ahlefeldt, J. G. Bartholomew, S. E. Beavan, S. M. Wittig, J. J. Longdell, and M. J. Sellars, Nature **517**, 177 (2015).

[6] T. Zhong, J. M. Kindem, J. G. Bartholomew, J. Rochman, I. Craiciu, E. Miyazono, M. Bettinelli, E. Cavalli, V. Verma, S. W. Nam, F. Marsili, M. D. Shaw, A. D. Beyer, and A. Faraon, Science **357**, 1392 (2017).

[7] M. Rančić, M. P. Hedges, R. L. Ahlefeldt, and M. J. Sellars, Nat. Phys. **14**, 50 (2018).

[8] B. Lauritzen, J. Minář, H. de Riedmatten, M. Afzelius, N. Sangouard, C. Simon, and N. Gisin, Phys. Rev. Lett. **104**, 080502 (2010).

[9] E. Fraval, M. J. Sellars, and J. J. Longdell, Phys. Rev. Lett. **95**, 030506 (2005).

[10] S. Probst, H. Rotzinger, S. Wünsch, P. Jung, M. Jerger, M. Siegel, A. V. Ustinov, and P. A. Bushev, Phys. Rev. Lett. **110**, 157001 (2013).

[11] X. Fernandez-Gonzalvo, Y.-H. Chen, C. Yin, S. Rogge, and J. J. Longdell, Phys. Rev. A **92**, 062313 (2015).

[12] A. M. Dibos, M. Raha, C. M. Phenicie, and J. D. Thompson, Phys. Rev. Lett. **120**, 243601 (2018).

[13] S. Chen, M. Raha, C. M. Phenicie, S. Ourari, and J. D. Thompson, Science **370**, 592 (2020).

[14] W. T. Carnall, G. L. Goodman, K. Rajnak, and R. S. Rana, J. Chem. Phys. **90**, 3443 (1989).

[15] C. Görller-Walrand and K. Binnemans, *Handbook on the Physics and Chemistry of Rare Earths*, edited by J. K. A. Gschneidner and L. Eyring (North-Holland, Amsterdam, 1996), Vol. 23, p. 121.

[16] D. J. Newman and B. K. C. Ng (Eds.), *Crystal Field Handbook* (Cambridge University Press, Cambridge, 2000).

[17] G. Liu, *Spectroscopic Properties of Rare Earths in Optical Materials*, edited by G. Liu and B. Jacquier (Springer Science & Business Media, 2006).

[18] A. A. Antipin, M. P. Davydova, M. V. Eremin, R. K. Luks, and A. L. Stolov, Opt. Spektrosk. **33**, 673 (1972).

[19] S. P. Horvath, J.-P. R. Wells, M. F. Reid, M. Yamaga, and M. Honda, J. Phys.: Condens. Matter **31**, 015501 (2018).

[20] S. P. Horvath, High-resolution spectroscopy and novel crystal-field methods for rare-earth based quantum information processing, Ph.D. thesis, University of Canterbury 2016.

[21] S. P. Horvath, J. V. Rakonjac, Y.-H. Chen, J. J. Longdell, P. Goldner, J. P. R. Wells, and M. F. Reid, Phys. Rev. Lett. **123**, 057401 (2019).

[22] N. L. Jobbitt, S. J. Patchett, Y. Alizadeh, M. F. Reid, J.-P. R. Wells, S. P. Horvath, J. J. Longdell, A. Ferrier, and P. Goldner, Phys. Solid State **61**, 780 (2019).

[23] B. A. Maksimov, V. V. Ilyukhin, Y. A. Khariton, and N. V. Belov, Sov. Phys. Crystallogr. **15**, 806 (1971).

[24] Y. Sun, T. Böttger, C. W. Thiel, and R. L. Cone, Phys. Rev. B **77**, 085124 (2008).

[25] J.-P. R. Wells, G. D. Jones, M. F. Reid, M. N. Popova, and E. P. Chukalina, Mol. Phys. **102**, 1367 (2004).

[26] K. N. Boldyrev, M. N. Popova, B. Z. Malkin, and N. M. Abishev, Phys. Rev. B **99**, 041105(R) (2019).

[27] M. Shiddiq, D. Komijani, Y. Duan, A. Gaita-Ariño, E. Coronado, and S. Hill, Nature **531**, 348 (2016).